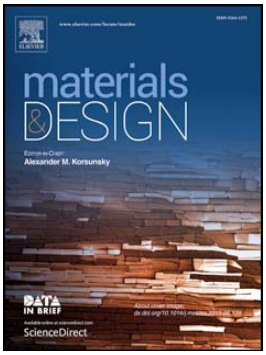

Selective laser melting of stainless steel 316L with low porosity and high build rates

Zhongji Sun, Xipeng Tan, Shu Beng Tor, Yee Yeong Wai

PII: S0264-1275(16)30637-2
DOI: doi: 10.1016/j.matdes.2016.05.035
Reference: JMADE 1783

To appear in:

Received date: 31 March 2016
Revised date: 6 May 2016
Accepted date: 11 May 2016

Please cite this article as: Zhongji Sun, Xipeng Tan, Shu Beng Tor, Yee Yeong Wai, Selective laser melting of stainless steel 316L with low porosity and high build rates, (2016), doi: 10.1016/j.matdes.2016.05.035

Selective laser melting of stainless steel 316L with low porosity and high build rates

Zhongji Sun, Xipeng Tan*, Shu Beng Tor, Wai Yee Yeong

Singapore Centre for 3D Printing, School of Mechanical and Aerospace Engineering, Nanyang Technological University, 50 Nanyang Avenue, Singapore 639798

*Corresponding author. E-mail: xptan1985@gmail.com or xptan@ntu.edu.sg

Abstract

The present study employs fast scanning speeds to fabricate high-density stainless steel 316L (SS316L) parts via selective laser melting (SLM). It aims to improve the production rate while maintaining a low porosity for the SLM-built parts. Density values of >99% were recorded for all the fabricated samples in this study. The scanning speed of the laser could be much improved due to the use of 380 W power laser. The overall build rate in this study is supposed to be enhanced by ~72% as compared to commonly used processing parameters. Detailed microstructural characterisation was carried out in order to obtain an in-depth understanding of the microstructure of SLM-built SS316L. The microhardness of built parts is between 213 to 220 HV, which is much higher than that of the standard annealed counterpart of ~155 HV. This study provides an insight on how to improve SLM build rates without any loss of parts' density and mechanical properties.

Keywords: additive manufacturing; selective laser melting; stainless steel 316L; transmission electron microscopy; microhardness

1. Introduction

Additive Manufacturing (AM), also known as three-dimensional (3D) Printing, has gathered much interest from both the industry and academia in the past few years. It is defined as a process of joining materials to make objects from a 3D model, usually layer upon layer, as opposed to subtractive manufacturing methodologies [1]. A wide range of materials such as metals, ceramics and polymers could be manufactured by various AM methods [2-4]. There are three AM methods that are commonly used for fabrication of metallic parts: (i) powder bed systems, (ii) powder feed systems and (iii) wire feed systems [4]. Selective laser melting (SLM) is an important powder bed based AM fusion technology. It utilises an energy source of laser to build parts by selectively melting a metallic powder bed in a layer-wise mode. Comparing to other non-powder bed based laser systems, such as engineered net shaping (LENS), SLM has the advantage of building complex geometries with a high resolution and a high accuracy [2]. Stainless steel 316L (SS316L) is one of the most widely investigated materials for SLM [5]. This is due to its wide applications in marine, biomedical equipment and fuel cell [6-8].

Kruth et al. carried out many pioneering studies on the SLM fabrications of stainless steels [9]. In 2004, they demonstrated the importance of different processing parameters for obtaining full-density metal parts via SLM [10]. Afterwards, many researchers validated their work [11-13]. However, it is very difficult to achieve full density of 100% in practice. This is because there will be inherent pores trapped within the powders. Moreover, unlike the moulding process, the lack of mechanical pressure makes SLM process more prone to bonding cracks between different layers [14]. One feasible way to achieve a high density is via the trial and error method. However, this process is very time consuming [15]. Several other methods were employed by different researchers. For instance, Yasa et al. investigated the effect of laser re-melting. They found that almost full density of 100% can be achieved when each layer was scanned twice [16]. However, scanning each layer twice increased the production time significantly. Recently, Cherry et al. made use of the semi-empirical formula of power energy density to enhance the density for SS316L parts. They proposed that a minimum porosity of 0.38% was obtained at an energy density of 104.52 J/mm^3 [17]. However, their work employed a laser power of <200 W. It is worth noting that most of the reported SLM fabrication processes made use of low power inputs, typically ≤200 W [15, 18]. Niendorf et al. reported the SLM fabrications of SS316L using powers of 400 W and 1000 W respectively [19]. However, no density information of the built parts was provided in their work. Thus, it remains unclear whether a high power input could yield a high density SS316L part via SLM.

The main advantage of using high power inputs is higher production rate. Slow build rate is one of the major limitations of SLM as compared to its counterparts such as electron beam melting (EBM). Buchbinder et al. demonstrated the possibility of using high power inputs to fabricate aluminium parts. Their work showed that using a high power input could improve the production rate by as much as 4 times [20]. However, they believed that high power inputs were only suitable for materials with high thermal conductivities like aluminium and copper if the beam diameter was kept constant. This is because spattering will occur if the input heat is not dissipated fast enough [20, 21]. In this study, SS316L parts were fabricated via SLM using a slightly higher power input of 380 W. It aims to achieve a higher build rate without losing the built parts' density. This work also provides detailed microstructural characterization and in-depth discussion on microstructure - microhardness relationship.

2. Experimental procedures

The SLM machine used in this work is SLM 250 HL (SLM Solutions, Germany). Figure 1(a) schematically illustrates the SLM 250 HL system. The focused spot size is ~80 μm when the employed laser power is below 400 W. During the fabrication process, recoater deposits powder across the build platform as it moves forward and backward. The excess of the deposited powder will be collected in two powder bottles located at the front and the back, and then recycled. A laser beam scans upon each layer of powder according to the input stereolithography (STL) file. It is controlled via the two rotating lenses above the F-theta lens. The build platform will move down with the lifting device by one layer's thickness after each scan. A new layer of powder is then deposited by the recoater. This process repeats itself until

the desired object is fabricated. The SS316L powder used in this work is shown in Figure 1(b). It is gas-atomised spherical powder in the range of 20 to 63 μm. The nominal chemical composition is (wt.%) 16-18% Cr, 10-14% Ni, 2-3% Mo, <0.03% C, <1% Si, <2% Mn, <0.045% P, <0.03% S, < 0.1 %N, and Fe balance.

There were 2 sets, 24 cubes fabricated by SLM in total for the present study. Each cube has a dimension of 10 × 10 × 10 mm^3. Their processing parameters are listed in Table 1. Laser power and layer thickness were fixed at 380 W and 50 μm, respectively. Scanning speed and hatch spacing were adjusted to make sure that the power energy density is close to 104.52 J/mm^3 as proposed by Cherry et al. [17]. The sample S01 has the fastest scanning speed of 3000 mm/s and the smallest hatch spacing of 25 μm among all the samples. The laser scanning speed decreases while hatch spacing increases from S01 to S12. The sample S12 has a scanning speed of 625 mm/s and a hatch spacing of 120 μm accordingly. The power energy density formula is $Q = \frac{P}{v \times h \times t}$, where Q is the power energy density, P is the power input, v is the scanning speed, h is the hatch spacing and t is the layer thickness. Laser scanning starts when the oxygen content in the build chamber was ≤0.05%. A bidirectional stripe scanning strategy was employed in this study. All the samples were built using the same stripe size of 1 mm.

The built parts' density was determined by both the image analysis method using optical microscopy (OM; ZEISS Axioskop 2 MAT) and the Archimedes method. The image analysis method evaluates the part's porosity by calculating the area percentage of pores on polished surfaces. The Archimedes method calculates the part's density based on the Archimedes Principle. The object's weight was measured in both air and ethanol. Given the ethanol's density, the part's density can then be obtained. Scanning electron microscopy (SEM; JEOL JMS 5600; 20 kV), X-ray diffraction (XRD; PANalytical Empyrean; Cu Kα; step size of 0.013°) and transmission electron microscopy (TEM; JEOL-2010; 200 kV) were used to examine the microstructure of the as-built SS316L samples. The samples were firstly ground with SiC-paper of grit #320 and followed by MD-Largo (DiaPro Largo 9 μm suspension). They were then polished with MD-Dac (DiaPro Dac 3 μm suspension) and MD-Nap (DiaPro Nap 1 μm suspension). Ralph's solution (100 ml H_2O, 200 ml methyl alcohol, 100 ml HCl, 2 g $CuCl_2$, 7 g $FeCl_2$ and 5 ml HNO_3) was adopted to etch the polished samples by swabbing for OM and SEM observations. Quantitative image analysis was carried out via the Image J software. TEM samples were manually ground down to ≤50 μm and then cut into discs of 3 mm in diameter. They were then prepared by ion milling with a beam voltage of 3.5 kV and a milling angle of 4 to 8°. Vickers microhardness (HV) measurements with 1 kg load and 15 s hold were conducted on metallographic samples using the Future Tech FM-300e microhardness tester. At least 10 microhardness measurements were taken for each sample with a standard deviation smaller than 5 HV.

3. Results

3.1. Porosity and melt tracks

The density measurement results by the image analysis method and the Archimedes method are shown in Figure 2(a). Both graphs show that a high density of >99% was achieved for all the SLM-built samples. However, the image analysis method records a higher value compared to the Archimedes method. Despite this minor difference, both graphs show a decreasing trend as it moves from samples S01 to S12, which can be seen from Figure 2(b) - (d). Only very small spherical pores were sporadically observed in the S01 sample. These spherical pores are likely to be caused by the trapped gas inside the SS316L precursor powder. The number of spherical pores increases from S01 to S06. Vertical cracks start to appear after S06 and the S12 sample has the most number of them, as shown in Figure 2(d). The possible reasons for the appearance of these vertical cracks will be discussed in the following section.

Figure 2(e) - (g) show the top surface topography of three representative samples. The distance between adjacent orange scan lines indicates the hatch spacing. They are 25, 60 and 120 μm for the S01, S06 and S12 samples respectively. There are some loose powder attached to the top surfaces for all the three samples. This might be because the suspended powder inside the build chamber fell down upon the top surfaces during melting. In addition, curved scanning tracks in each stripe can be observed for all the samples. This is because of the bidirectional stripe scanning strategy. As laser scanned in "snake" shape on the x-y plane, e.g. from left to right along stripe direction, heat loss towards two sides was restricted due to the previous and the subsequent hot scanning lines. While the heat was easily dissipated from two ends. As a result, the two ends of a scanned track were firstly solidified, and at the same time its middle section still could be kept in fluid and move a bit towards the subsequent hotter scanning line due to the surface tension effect. Thus, all the scanning tracks were curved and pointed towards the overall scanning direction. As the hatch spacing increases from 25 to 120 μm, the top surfaces become increasingly rough. One possible reason is that when hatch spacing is small, the re-melting area of newly scanned lines helps to smoothen the previous scanned lines. Therefore, large hatch spacing is not favourable to the top surface's finish.

Figure 3 shows an image of layer-wise melt tracks for the S01 sample. Most of the melt tracks seems to be uneven and irregular. There are three different kinds of melt track morphologies in general. The melt tracks in Figure 3(i) are parallel to the horizontal line and they stack on top of one another. This is owning to the fact that the red scanning lines were scanned parallel to the horizontal line from right to left. The distance between the melt tracks in Figure 3(ii) is wider than that in Figure (iii) but both of them are perpendicular to the horizontal line as the scanning lines in Figure 3(iii) were scanned perpendicular to the horizontal line. The distance between the melt tracks in Figure 3(iii) is the actual hatch spacing of 25 μm. Due to a change in scanning direction, the scanning lines in Figure 3(ii) are further away from one another, resulting in the wide melt tracks.

3.2. Phase identification and microstructure

Figure 4 reveals that there are two main phases in the SLM-built SS316L samples, i.e. face-centred cubic (fcc) austenite (γ phase) and body-centred cubic (bcc) ferrite (δ phase). No

martensite formed below 4 K if no strain was applied [22]. This helps to further confirm that there should be no martensitic phase formed in the SLM-built SS316L samples. The diffraction patterns of the S01 and S12 samples show wider peaks compared to those of the precursor powder. It indicates the presence of residual stresses within the S01 and S12 samples after SLM process, which causes the lattice distortions that result in obvious peak widening phenomenon [23, 24].

Figure 5 shows the typical cellular sub-grain microstructures in the S01 sample. Epitaxial growth is evident as grains can grow across melt tracks. It is found that there is no obvious difference on the cellular size among the S01-S12 samples. The average cell size was determined to be ~1 ± 0.5 μm. In order to examine the sub-grain microstructure and the retained δ phase in detail, TEM studies were carried out. Figure 6 shows the cellular microstructure of γ that was confirmed with the inserted selected area electron diffraction (SAED) pattern. It can be clearly observed that each cell was surrounded with dense, entangled dislocations.

Figure 7 shows the bright field TEM images of the retained phase in the S01 sample. Acicular phases were observed within the γ austenite matrix as shown in Figure 7(a). The big acicular phase has a length of ~3.2 μm passing through several cells. The diffraction pattern in the zone axis of <111> confirms that the retained acicular phase is δ ferrite with a bcc structure. The δ ferrite phase in SLM-built SS316L has previously been identified by Saeidi et al.'s EBSD study [25]. It is known that δ ferrite is the high-temperature bcc phase for the microstructure of SS316L. Due to the fast cooling rate involved in SLM process, a small amount of δ ferrite retained without transforming to the low-temperature γ austenite phase. The retained δ phase is supposed to strengthen the soft austenitic matrix.

A grain boundary is present between two grains with different contrast in Figure 7(a). The δ ferrite phase was observed to be randomly distributed within the matrix. In addition to the acicular morphology, δ ferrite was also found to have various irregular shapes (see Figure 7(b) and 7(c)). Apart from the retained δ ferrite, a large amount of spherical particles having a size range of ~100-200 nm was observed under TEM. They were found to be amorphous in terms of the diffuse diffraction rings in Figure 8. Their compositions were analysed using TEM-EDX with a result of 36% O, 40% Si, 10% Cr, 14% Mn (in at.%). Therefore, the nano-scale inclusions are suggested to be the silicate containing chromium and manganese, which is agreement with the previous work [25]. They are believed to resist dislocation movement and hence much strengthen the materials.

3.3. Microhardness

The Vickers microhardness results for the SLM-fabricated samples are shown in Figure 9. It shows a decreasing trend from samples S01 to S12 overall with the highest value of 220 HV in the S01 sample and the lowest value of 213 HV in the S12 sample. By contrast, the microhardness of annealed SS316L is in the range of 150 to 160 HV [26], as shown in the shaded block in Figure 9.

4. Discussion

By utilising a laser power input of 380 W, as compared to the most commonly used power input of ~100 W before, the scanning speed of the laser can be improved by ~3.8 times according to the power energy density formula while other parameters remain the same. The SLM process cycle time is divided into primary and auxiliary process time. The primary process time mainly consists of the laser's scanning time. While the auxiliary process time accounts for the powder recoating and substrate movement time [27]. It is found that in order to fabricate the 24 ($10 \times 10 \times 10$ mm^3) cubes, 380W laser can save ~41.8% of the total build time (from 11h:29m:16s to 6h:40m:58s, simulated by the built-in software of SLM 250 HL machine) as compared to 100 W laser. This translates to an increase in the build rate by 72%, i.e. from 0.6 mm^3/s to 1.0 mm^3/s. Thus this reduction in the primary process time can help improve the overall production rate significantly. Furthermore, since the auxiliary process time depends on the hardware and mechanisms of different machines, it is also easier to improve the overall production rate by reducing the primary process time via a higher power input.

The scanning strategy used for this study helps to achieve good fusion bonding and effectively reduce porosity. The short stripe length of 1 mm is used to prevent surface swelling. The constant change of scanning direction for consecutive layers ensures good fusion bonding between layers and minimises the residual stresses. However, even for the SLM-fabricated samples with the same scanning strategy and the same energy density input, slight change in the scanning parameters is found to affect the porosity. The samples, built with higher scanning speeds and smaller hatch spacing, tend to have lower porosities. This is due to the presence of vertical cracks observed from samples S07 to S12 in this work. One of the possible reasons for the formation of these vertical cracks was explained by Cloots et al. for SLM-fabricated In738LC alloy [28]. It was proposed that when the scanning speed was low, the laser penetration depth would increase. Inhomogeneous rapid solidification resulted in constitutional undercooling. This in turn created thin films with a low melting point between different grains. Residual tensile stresses could not be transmitted through the brittle grain boundaries and shrinkage occurred [28]. Another possible reason for the vertical cracks is due to the so-called "keyhole effect" [29]. Voids might be generated when the laser penetration depth increased. This is further supported by Wayne et al.'s work on SLM-built SS316L [29] and Thijs et al.'s work on SLM-built AlSi10Mg alloy [30]. Moreover, the increasing thermal gradient caused by the slow scanning speeds may also be a reason for the appearance of those vertical cracks. The vertical cracks can propagate more than one-layer thickness as observed in Figure 2(d). This may be due to the fact that the cracks developed from previously deposited layers served as the nucleation sites for the ones occurred in the subsequent layers. It is noted that all the 12 samples were built with the same energy density of ~104 J/mm^3 while they contain different porosities. Thus, an optimal energy density is only the necessary condition to ensure a high density. Some other influencing factors, e.g. laser penetration depth and hatch line spacing, are also needed to be taken into consideration in order to achieve fully dense SLM-built parts.

The microstructure of SLM-built SS316L in this study is very complex as shown in Figure 5. Grains with different orientations are present even under the same melt track. This

might be due to the continuous re-melting process such that the grain growth direction constantly changes according to the heat flow directions. The Marangoni effect further affects the microstructure as the different heat flow directions exist within the same molten pool, creating different grain growth orientations [31]. The columnar grains with cellular structure are believed to form mainly due to the high thermal gradient and the high solidification rate accompanied with SLM process. This kind of microstructure has been observed for many different materials processed by SLM, e.g. SS316L, and Cobalt alloy [16, 32]. Moreover, the solidification map developed for titanium alloy further confirms that columnar microstructure will occur when the thermal gradient is $\geq 10^4$ K/cm [33]. High thermal gradient is a characteristic of SLM process. It was reported that the thermal gradient for SLM process could be as high as 10^6 K/m [30]. Therefore, most of the materials fabricated by SLM may have a columnar microstructure. The cellular sub-grain boundaries were reported to be rich in molybdenum [25]. The large size of molybdenum atoms creates severe crystal lattice distortions. This in turn generates many dislocations (as shown in Figure 6), which will help to increase the hardness of the SLM-built parts (see Figure 9).

It was proposed that for austenitic stainless steels, the cooling rate $\dot{T}$ could be calculated from the primary cellular spacing λ_1 according to the equation $\lambda_1 = 80\dot{T}^{-0.33}$ [34]. Therefore, the average cell size of ~1 μm observed in this work corresponds to a cooling rate of ~5.8×10^5 K/s. The average cell size in Saeidi et al.'s work is 0.5 μm, which corresponds to a cooling rate of ~4.8×10^6 K/s. Provided this variation in the cell size is due to different cooling rates. It may be the result of different build heights between the two studies. It is worth noting that the build height of 10 mm in this work is much higher compared to the build height of 2 mm in Saeidi et al.'s work. Obviously the cooling rate will be higher in the shorter builds as they were directly built on base plate. The fine cellular size is the main reason for the SLM-built samples to have high harnesses and high strengths.

The microhardness results obtained in this work (~216 HV) are much higher compared to those of the annealed counterparts (~155 HV) as mentioned above. However, they are still significantly lower compared to the 325 HV reported by Saeidi et al. using a similar SLM process [35]. It is suggested that this is due to the difference both in cellular size and the quantity of the amorphous nano-scale inclusions. The average cellular size in Saeidi et al's work is slightly smaller compared to that of the present study due to their faster cooling rates, leading to a much higher microhardness for their SLM-built samples. Moreover, the nano-scale inclusions observed in their work are much more in quantity compared to those in this work. Since the amorphous nano-scale inclusion has been identified as a silicate, and the precursor SS316L powder does not have oxygen, the oxygen content within the build chamber will be the key factor in determining the quantity of nano-scale inclusions. Of particular note is that the oxygen content should be <0.05% when the laser started to scan and it stabilised at ~0.16% after several layers' scanning in the present work. This is because the trapped air inside the powder bed entered the build chamber and argon was brought in periodically to balance it off. In addition to the oxygen content within the build chamber, inappropriate powder storage method or humid build environment may also result in oxygen

pickup. All the above mentioned situations will result in difference in the quantity of nano-scale inclusions obtained at the end of the SLM build.

However, it still remains unclear which factor contributes the most to the microhardness variations of the SLM-fabricated SS316L samples. Both the oxygen content and the microstructure scale could have a significant influence. Nevertheless, it will be interesting to know the relationship between the oxygen content and the obtained microhardness values. This is because oxide dispersed steels (ODS) could be built with the desired microhardness simply by controlling the oxygen content within the build chamber. Moreover, the build of gradient ODS will also be possible for SLM if the oxygen content within the chamber could be precisely controlled during the whole manufacturing process.

5. Conclusions

High-density SS316L parts were successfully built via SLM with high build rates in this work. The following conclusions can be drawn:

a) There is a direct relationship between the laser power input and the build rate for SLM process. Comparing to the normally employed power input, such as 100 W, the scanning speed of the laser can be enhanced by ~3.8 times using 380 W and the overall build rate could be improved by ~72%. Therefore, increasing the power input of the laser is a very important measure to increase the build rate of SLM process.

b) High density of SS316L parts can be maintained while increasing the SLM build rate. All the SLM-built SS316L parts in the present study have high densities of >99%, due to the use of appropriate scanning strategy and scanning parameters. It is recommended to find out a suitable power energy density for a material and then adjust the scanning strategy or scanning parameters catering to the increase in power input. Moreover, vertical cracks should be avoided in order to achieve a high density.

c) The two main phases present in the SLM-built SS316L are the primary fcc γ austenite and the small amount of retained bcc δ ferrite. The microhardness of SLM-built SS316L is believed to be significantly affected by the dislocation density and the quantity of the nano-scale amorphous inclusions. The SLM-built SS316L parts were found to have a microhardness value in the range of 220 to 213 HV, which is much higher compared to the annealed SS316L counterpart.

Acknowledgements

The authors are grateful to Kok Yihong, Toh Wei Quan and Tan Yu Jun who are the Ph.D. students in our centre for their help with the SLM fabrication and the fruitful discussion.

References

[1] ASTM I. Standard Terminology for Additive Manufacturing Technologies. F2792-12a2009.
[2] Frazier WE. Metal additive manufacturing: A review. Journal of Materials Engineering and Performance. 2014;23:1917-28.
[3] Eckel ZC, Zhou C, Martin JH, Jacobsen AJ, Carter WB, Schaedler TA. Additive manufacturing of polymer-derived ceramics. Science. 2016;351:58-62.
[4] Gibson I, Rosen DW, Stucker B. Additive manufacturing technologies: Springer; 2010.
[5] Miranda G, Faria S, Bartolomeu F, Pinto E, Madeira S, Mateus A, et al. Predictive models for physical and mechanical properties of 316L stainless steel produced by selective laser melting. Materials Science and Engineering: A. 2016.
[6] Dewidar MM, Khalil KA, Lim J. Processing and mechanical properties of porous 316L stainless steel for biomedical applications. Transactions of Nonferrous Metals Society of China. 2007;17:468-73.
[7] Wang H, Sweikart MA, Turner JA. Stainless steel as bipolar plate material for polymer electrolyte membrane fuel cells. Journal of Power Sources. 2003;115:243-51.
[8] Xu F-l, Duan J-z, Lin C-g, Hou B-r. Influence of Marine Aerobic Biofilms on Corrosion of 316L Stainless Steel. Journal of Iron and Steel Research, International. 2015;22:715-20.
[9] Kruth J-P, Mercelis P, Van Vaerenbergh J, Froyen L, Rombouts M. Binding mechanisms in selective laser sintering and selective laser melting. Rapid prototyping journal. 2005;11:26-36.
[10] Kruth JP, Froyen L, Van Vaerenbergh J, Mercelis P, Rombouts M, Lauwers B. Selective laser melting of iron-based powder. Journal of Materials Processing Technology. 2004;149:616-22.
[11] Yadroitsev I, Bertrand P, Smurov I. Parametric analysis of the selective laser melting process. Applied surface science. 2007;253:8064-9.
[12] Meier H, Haberland C. Experimental studies on selective laser melting of metallic parts. Materialwissenschaft und Werkstofftechnik. 2008;39:665-70.
[13] Zhang B, Liao H, Coddet C. Effects of processing parameters on properties of selective laser melting Mg–9% Al powder mixture. Materials & Design. 2012;34:753-8.
[14] Kruth J-P, Badrossamay M, Yasa E, Deckers J, Thijs L, Van Humbeeck J. Part and material properties in selective laser melting of metals. Proceedings of the 16th International Symposium on Electromachining2010.
[15] Kamath C, El-dasher B, Gallegos GF, King WE, Sisto A. Density of additively-manufactured, 316L SS parts using laser powder-bed fusion at powers up to 400 W. The International Journal of Advanced Manufacturing Technology. 2014;74:65-78.
[16] Yasa E, Kruth JP. Microstructural investigation of Selective Laser Melting 316L stainless steel parts exposed to laser re-melting. Procedia Engineering. 2011;19:389-95.
[17] Cherry JA, Davies HM, Mehmood S, Lavery NP, Brown SGR, Sienz J. Investigation into the effect of process parameters on microstructural and physical properties of 316L stainless steel parts by selective laser melting. The International Journal of Advanced Manufacturing Technology. 2014;76:869-79.
[18] Wu W, Tor SB, Chua CK, Leong KF, Merchant A. Investigation on processing of ASTM A131 Eh36 high tensile strength steel using selective laser melting. Virtual and Physical Prototyping. 2015;10:187-93.
[19] Niendorf T, Leuders S, Riemer A, Richard HA, Tröster T, Schwarze D. Highly Anisotropic Steel Processed by Selective Laser Melting. Metallurgical and Materials Transactions B. 2013;44:794-6.
[20] Buchbinder D, Schleifenbaum H, Heidrich S, Meiners W, Bültmann J. High power selective laser melting (HP SLM) of aluminum parts. Physics Procedia. 2011;12:271-8.

[21] Liu Y, Yang Y, Mai S, Wang D, Song C. Investigation into spatter behavior during selective laser melting of AISI 316L stainless steel powder. Materials & Design. 2015;87:797-806.
[22] Spencer K, Embury JD, Conlon KT, Véron M, Bréchet Y. Strengthening via the formation of strain-induced martensite in stainless steels. Materials Science and Engineering: A. 2004;387-389:873-81.
[23] Leuders S, Thöne M, Riemer A, Niendorf T, Tröster T, Richard H, et al. On the mechanical behaviour of titanium alloy TiAl6V4 manufactured by selective laser melting: Fatigue resistance and crack growth performance. International Journal of Fatigue. 2013;48:300-7.
[24] Kok Y, Tan XP, Tor SB, Chua CK. Fabrication and microstructural characterisation of additive manufactured Ti-6Al-4V parts by electron beam melting. Virtual and Physical Prototyping. 2015;10:13-21.
[25] Saeidi K, Gao X, Zhong Y, Shen ZJ. Hardened austenite steel with columnar sub-grain structure formed by laser melting. Materials Science and Engineering: A. 2015;625:221-9.
[26] Woldman NE, Frick JP. Woldman's Engineering Alloys: ASM International; 2000.
[27] Schleifenbaum H, Meiners W, Wissenbach K, Hinke C. Individualized production by means of high power Selective Laser Melting. CIRP Journal of manufacturing science and technology. 2010;2:161-9.
[28] Cloots M, Uggowitzer PJ, Wegener K. Investigations on the microstructure and crack formation of IN738LC samples processed by selective laser melting using Gaussian and doughnut profiles. Materials & Design. 2016;89:770-84.
[29] King WE, Barth HD, Castillo VM, Gallegos GF, Gibbs JW, Hahn DE, et al. Observation of keyhole-mode laser melting in laser powder-bed fusion additive manufacturing. Journal of Materials Processing Technology. 2014;214:2915-25.
[30] Thijs L, Kempen K, Kruth J-P, Van Humbeeck J. Fine-structured aluminium products with controllable texture by selective laser melting of pre-alloyed AlSi10Mg powder. Acta Materialia. 2013;61:1809-19.
[31] Wang D, Song C, Yang Y, Bai Y. Investigation of crystal growth mechanism during selective laser melting and mechanical property characterization of 316L stainless steel parts. Materials & Design. 2016;100:291-9.
[32] Takaichi A, Nakamoto T, Joko N, Nomura N, Tsutsumi Y, Migita S, et al. Microstructures and mechanical properties of Co–29Cr–6Mo alloy fabricated by selective laser melting process for dental applications. Journal of the mechanical behavior of biomedical materials. 2013;21:67-76.
[33] Kobryn P, Semiatin S. Microstructure and texture evolution during solidification processing of Ti–6Al–4V. Journal of Materials Processing Technology. 2003;135:330-9.
[34] Schubert T, Löser W, Schinnerling S, Bächer I. Alternative phase formation in thin strip casting of stainless steels. Materials science and technology. 1995;11:181-5.
[35] Saeidi K, Kvetková L, Lofaj F, Shen Z. Austenitic stainless steel strengthened by the in situ formation of oxide nanoinclusions. RSC Adv. 2015;5:20747-50.

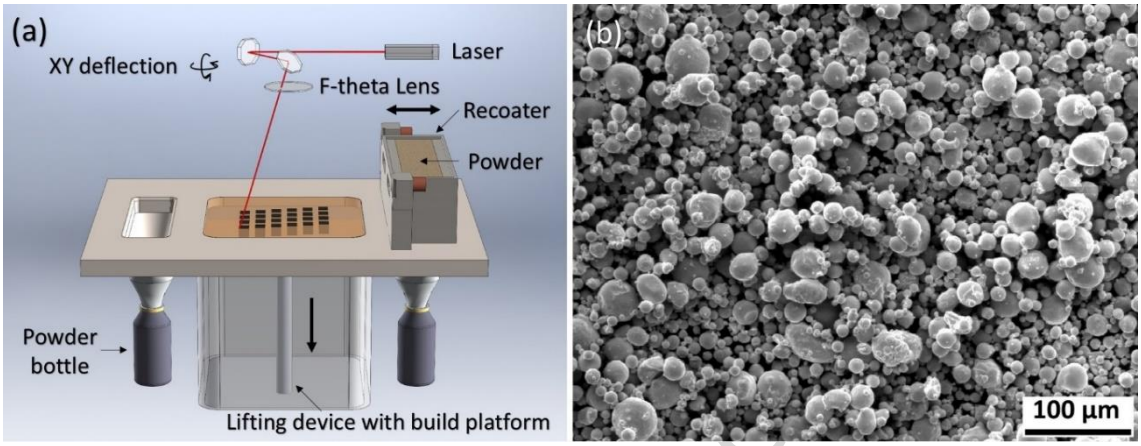

Figure 1. (a) Schematic of SLM 250 HL system. (b) Micrograph of SS316L powder.

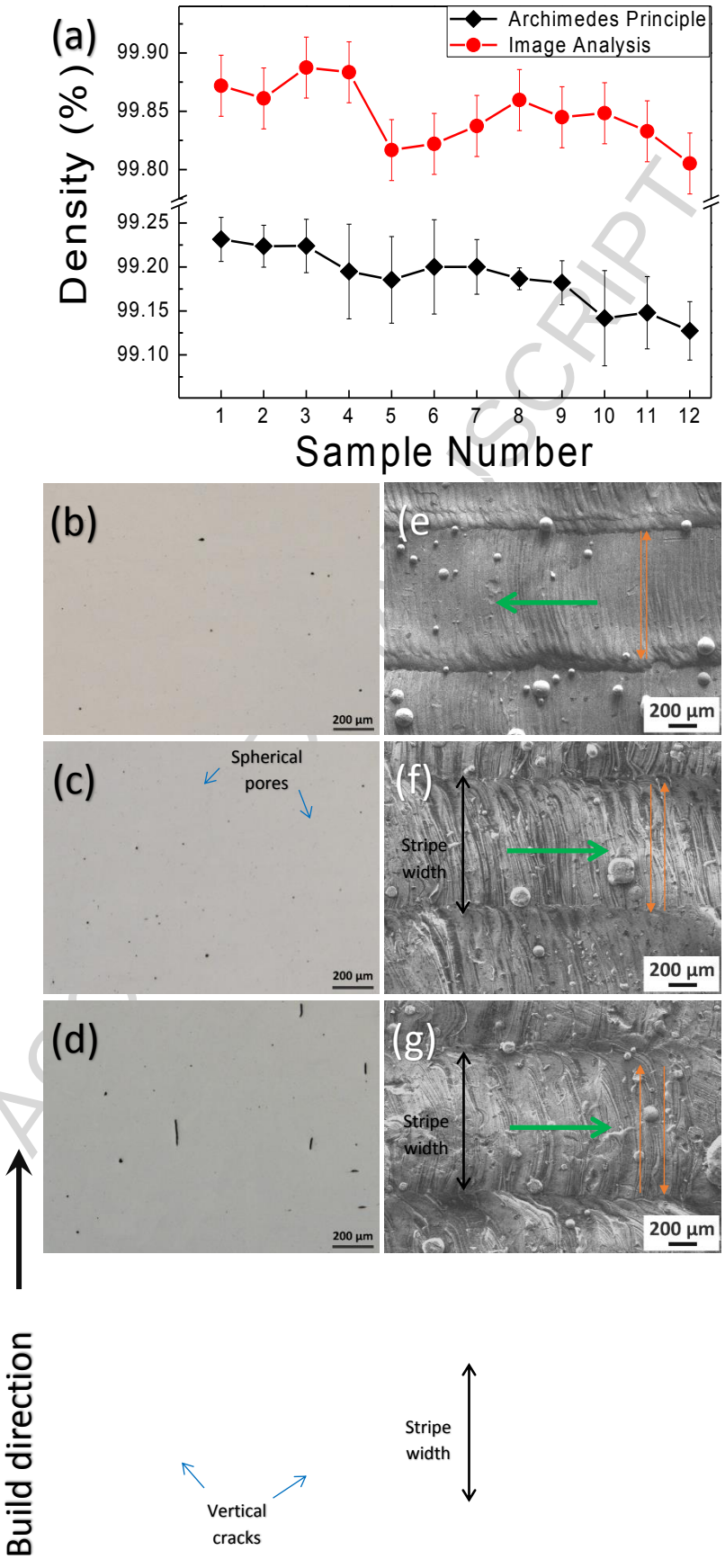

Figure 2. (a) Density graphs obtained from Archimedes and image analysis methods. The OM images of (b) S01 (c) S06 (d) S12 showing the pores. Build direction is indicated for (a), (b) and (c). SEM images showing the topography of (e) S01 (f) S06 (g) S12. The green arrows point towards the overall scanning directions and the orange arrows illustrate the two adjacent scanning lines.

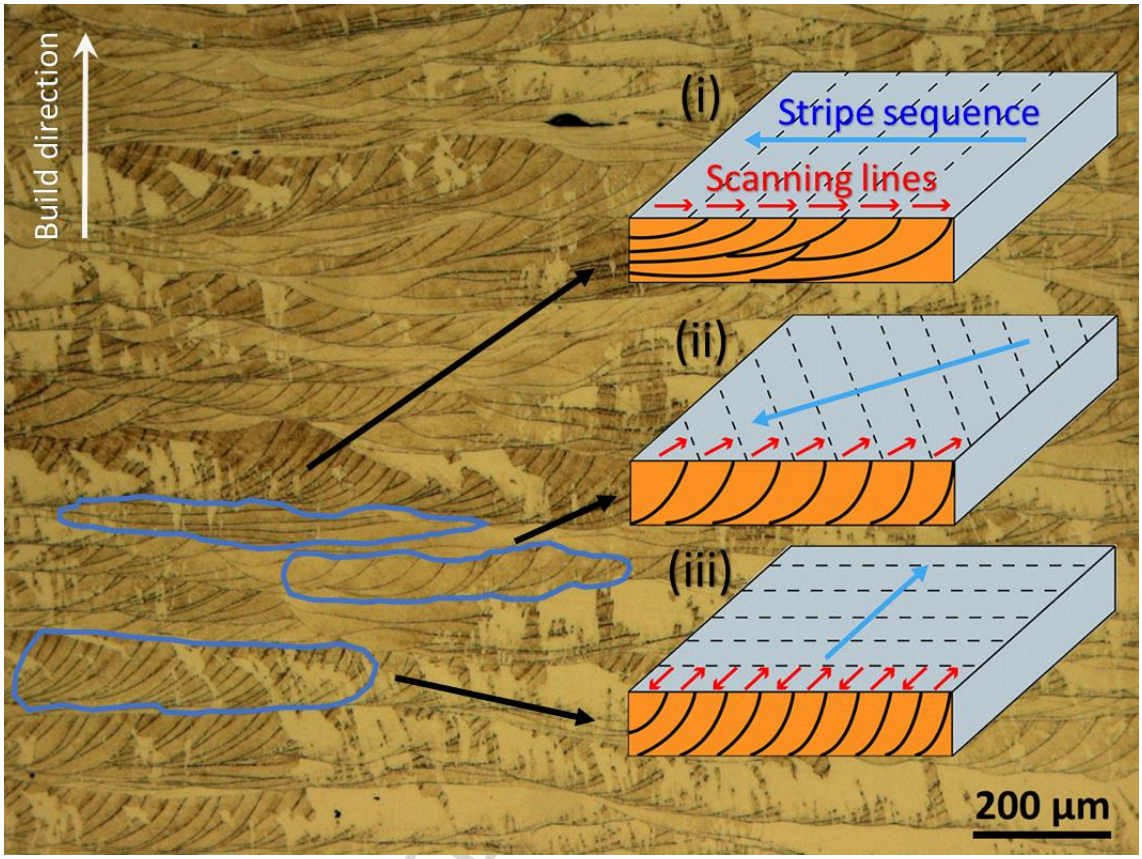

Figure 3. Relationship between scanning strategy and melt track morphology for the S01 sample. Insets (i), (ii) and (iii) illustrate the formation of different melt tracks. Build direction is indicated.

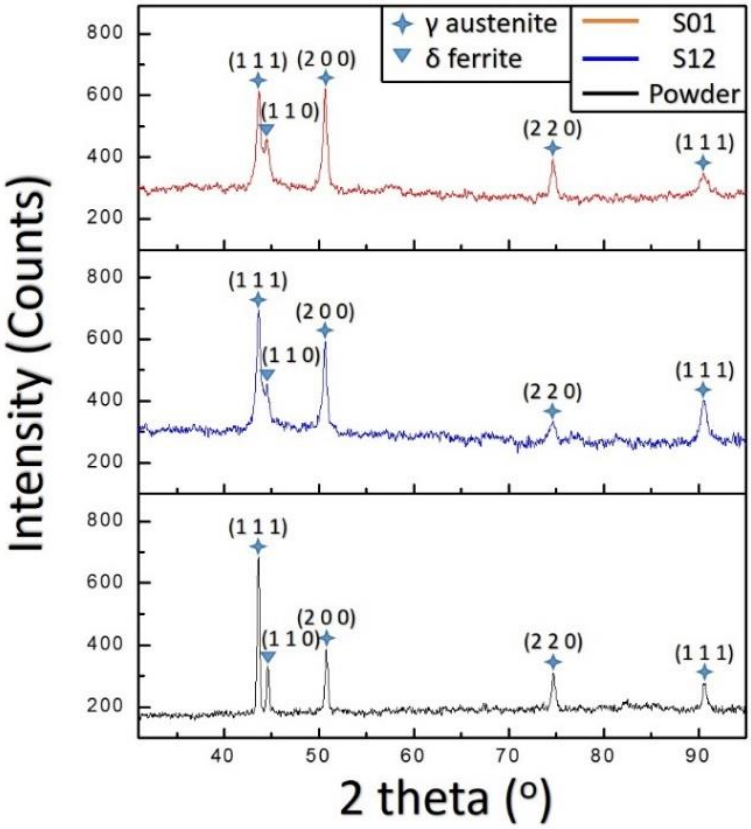

Figure 4. XRD profiles for S01, S12 and SS316L powder.

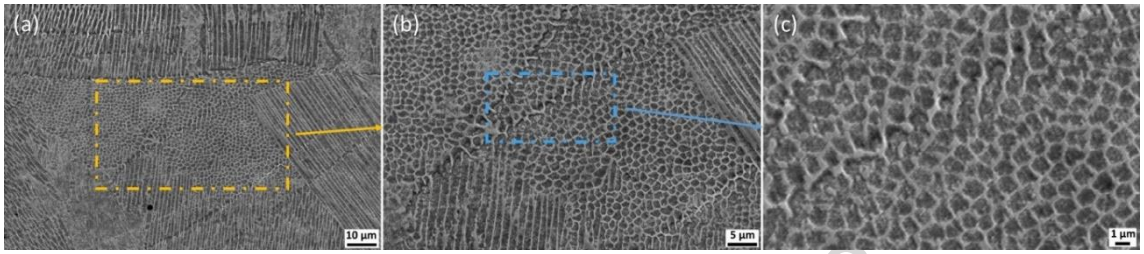

Figure 5. SEM images of the S01 sample (a) showing the cellular microstructure. (b) & (c) Enlarged views of (a).

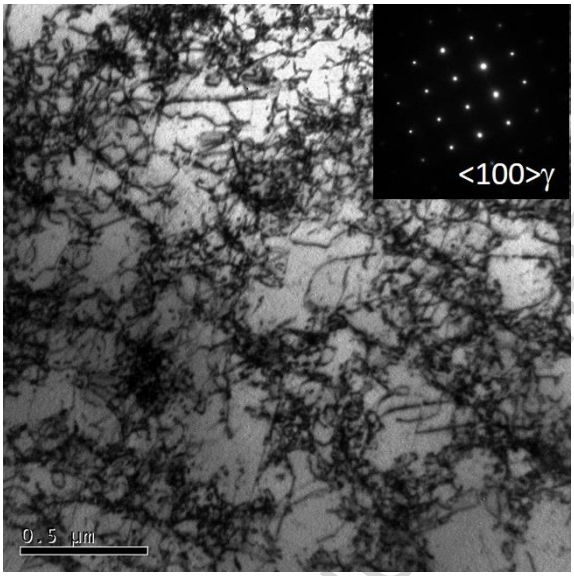

Figure 6. TEM image showing the cellular microstructures of the S01 sample. The inset of SAED pattern indicates γ austenite matrix.

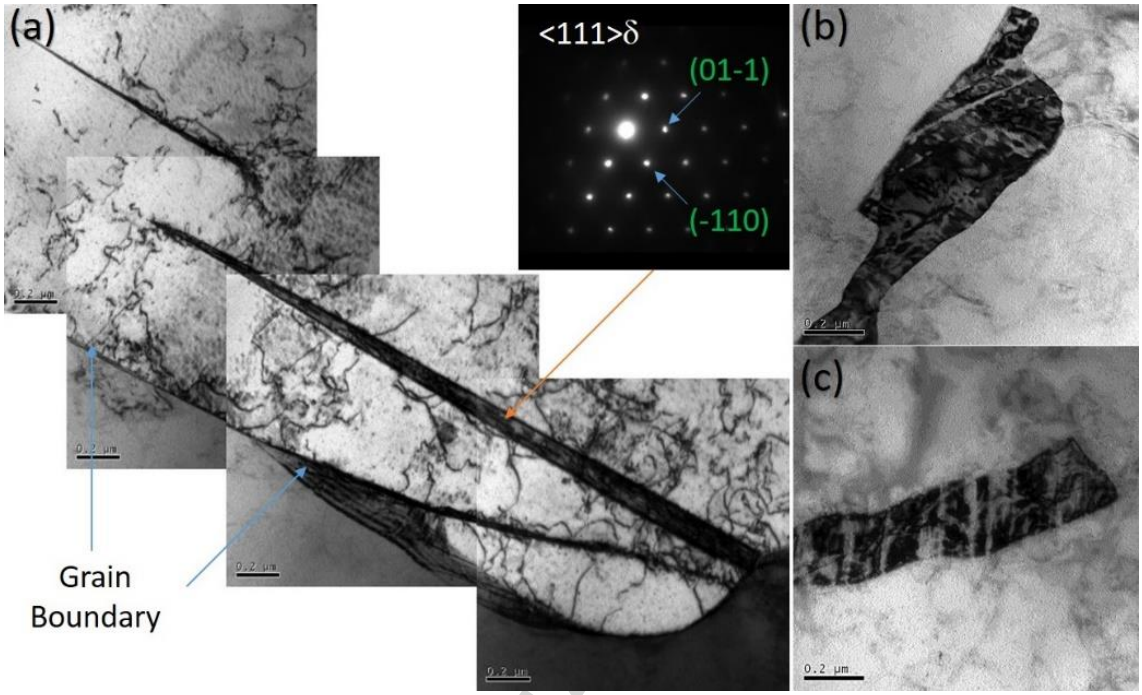

Figure 7. TEM images of δ ferrite (a) Acicular ferrite with SEAD pattern (b) and (c) Irregular-shaped ferrites.

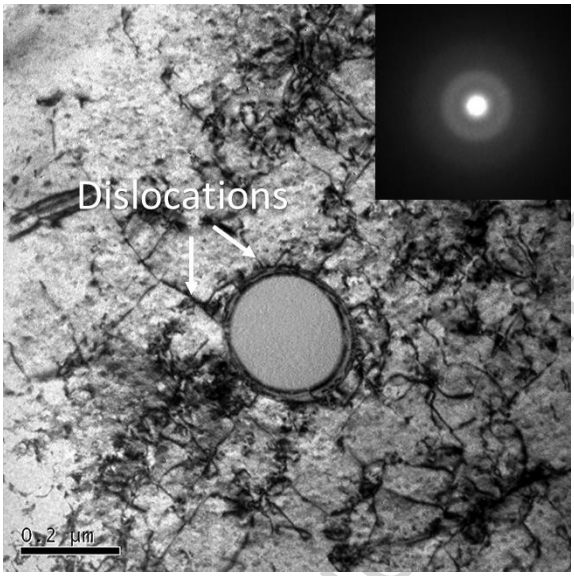

Figure 8. TEM image of a spherical inclusion. The inset of the diffuse ring pattern indicates that it is amorphous.

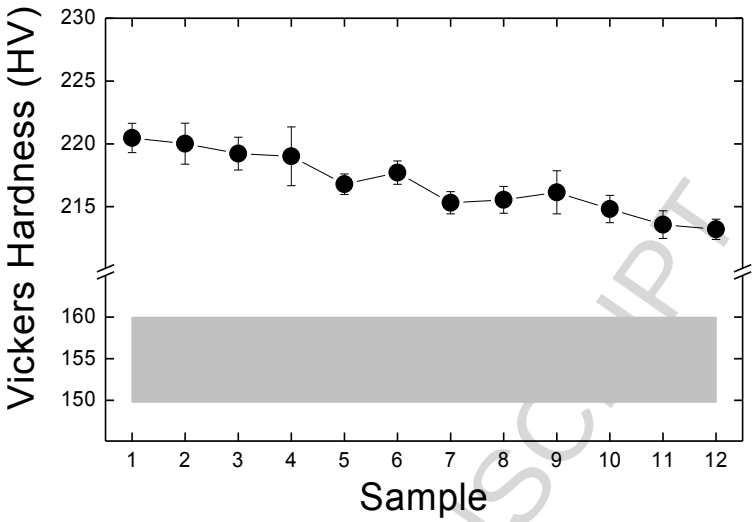

Figure 9. Vickers microhardness graph for samples from S01 to S12, with the annealed SS316L's microhardness range shown in the block region below.

Table 1 SLM parameters for the fabrication of SS316L samples.

Sample	Laser power [W]	Layer thickness [µm]	Scanning speed [mm/s]	Hatch spacing [µm]	Energy Density [J/mm^3]
S01	380	50	3000	25	101.33
S02	380	50	2500	30	101.33
S03	380	50	2000	35	108.57
S04	380	50	1750	40	108.57
S05	380	50	1500	50	101.33
S06	380	50	1250	60	101.33
S07	380	50	1050	70	103.40
S08	380	50	950	80	100.00
S09	380	50	850	90	99.35
S10	380	50	750	100	101.33
S11	380	50	700	110	98.70
S12	380	50	625	120	101.33

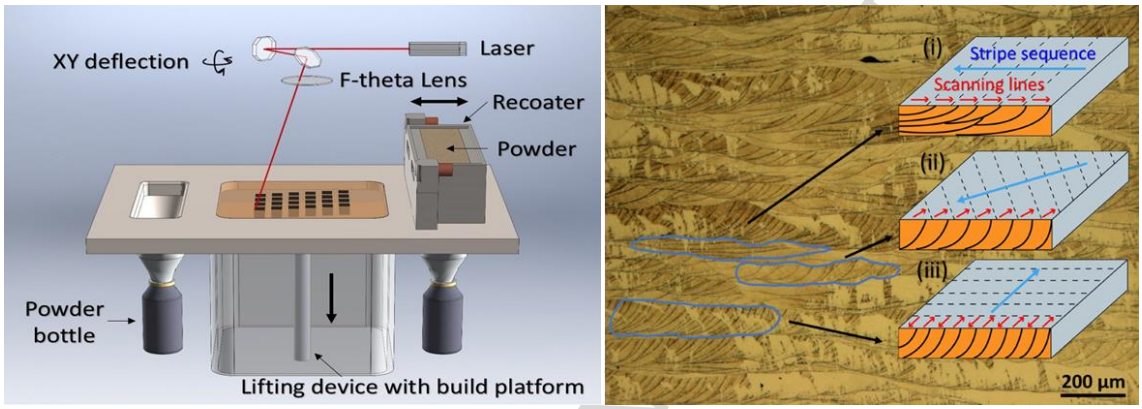

Graphical abstract

Highlights

- High-density SS316L parts were successfully built via SLM
- Build rate was significantly improved without sacrificing parts' density
- The relationship between microstructure and microhardness was investigated
- An alternative way to develop SLM processing parameters for new materials was suggested